PCCP

PAPER

View Article Online
View Journal | View Issue

Cite this: *Phys. Chem. Chem. Phys.*, 2019, **21**, 11351

Varying oxygen coverage on Cu_{55} and its effect on CO oxidation†

Li Ma [a] and Jaakko Akola *[ab]

Received 18th February 2019,
Accepted 7th May 2019

DOI: 10.1039/c9cp00974d

rsc.li/pccp

Adsorption of molecular oxygen on a Cu_{55} cluster and the resulting oxidation effects have been investigated by spin-polarized density functional theory (DFT). The optimal structure for each $Cu_{55}O_{2N}$ (N = 1–20) complex has been obtained *via* a sequential addition of O_2 and systematic screening of the preferable adsorption sites. Upon structural optimization, several O_2 molecules dissociate readily on Cu_{55} at different oxygen coverages, and further DFT molecular dynamics simulations at 300 K confirm the instability (small dissociation barrier) of the remaining O_2 and a spontaneous movement of some oxygen atoms from the surface sites towards the cluster interior. The Cu_{55} cluster and its oxidized derivatives have been placed on a γ-Al_2O_3(100) surface to study the cluster–support interaction, and furthermore, CO oxidation reactions on both $Cu_{55}(O)_{2N}$ and $Cu_{55}(O)_{2N}/\gamma$-Al_2O_3(100) have been studied as a function of oxygen coverage. The CO oxidation reaction barrier is rather insensitive to the oxygen coverage regardless of the support, indicating a small increase in activity with the number of surface oxygen atoms.

1. Introduction

The application of nanoparticles in heterogeneous catalysis is an active area of research. Noble metals, in particular the platinum group metals (PGMs) such as Pd, Pt, Ru, and Rh, have shown high activities and good stabilities for many reactions.[1–4] However, they are classified as critical metals owing to their high cost, limited availability, and socio-economic issues related to mining processes and supply (environment, working conditions, *etc.*). This has motivated the active search for more abundant metal catalysts with similar and/or improved performance characteristics for PGM replacement. Such catalysts are highly desirable for a wide variety of applications, not only in heterogeneous catalysis (*e.g.* acetylene hydrogenation[5] and ammonia decomposition[6]) but also in electrochemistry (hydrogen energy and CO_2 reduction).[7] Here, Cu-based catalysts have attracted considerable attention due to their low cost (earth-abundant) and a variety of industrial applications, including hydrogenation,[8] oxidation[9] and synthesis of methanol.[10] Much work has been performed over a number of years to optimize their performance. However, under industrial conditions, the catalyst surfaces are readily covered by the reactant, intermediate and product species causing issues with stability. The existence of the adsorbed species or layers may significantly affect the adsorption behavior of other species and reaction mechanisms or induce catalyst reconstruction.

It is well known that the CO oxidation reaction mechanism on a catalyst is influenced by the reactant gas coverage. Under high O_2 pressure, surface oxides have been proposed as the active phases for late-transition and noble metal elements,[11–13] which contradicts the well-accepted opinion that the transition or noble metal *per se* is responsible for CO oxidation. At low CO coverage, dissociated oxygen is the active species for the production of CO_2 from CO, whereas at higher CO coverage, molecular O_2 can directly react with CO *via* the formation of an OOCO intermediate.[14] Such studies of CO oxidation on transition metal surfaces and supported particles under varying partial pressures are beneficial for understanding the reaction mechanisms under realistic or industrial conditions and also for providing insight on the changing activity on metal surfaces or particles (catalyst stability).

Concerning the adsorption of oxygen on Cu catalysts, most studies have considered only a single O_2 molecule.[15–17] The effects

[a] *Computational Physics Laboratory, Tampere University, P.O. Box 692, FI-33014 Tampere, Finland*
[b] *Department of Physics, Norwegian University of Science and Technology, NO-7491 Trondheim, Norway. E-mail: jaakko.akola@ntnu.no*

† Electronic supplementary information (ESI) available: Details of stepwise adsorption of O_2 molecules; optimized geometries of Cu_{55} and Cu_{55}/γ-Al_2O_3(100) (Fig. S1); geometries of $Cu_{55}O_{2N}$ with the number of O_2 dissociation increasing from zero to seven (Fig. S2); The full set of geometries for the stepwise adsorption of O_2 molecules (N = 1–20) on Cu_{55} (Approach 1) (Fig. S3); geometries of $Cu_{55}O_{2N}$ (N = 10) at 0 K and after 20 ps of MD at 300 K (Fig. S4); adsorption energy $E_a(N)$ of each O_2 and average adsorption energy $\langle E_a(N)\rangle$ of added O_2 molecules *versus* the number of O_2 added on the Cu_{55} cluster (Approach 1) (Fig. S5); properties of the stepwise O_2 adsorption complexes $Cu_{55}O_{2N}$ (N = 1–20, Approach 1) (Table S1); the full set of geometries for stepwise adsorption and dissociation of O_2 molecules (N = 1–20) on Cu_{55} (Approach 2) (Fig. S6); spin-polarized Cu_{55} d-projected density of states (d-PDOS) with $(O)_{2N}$ (N = 1, 10, and 20) coverage (Fig. S7); properties of the stepwise O_2 adsorption and dissociation complexes $Cu_{55}O_{2N}$ (N = 1–20, Approach 2) (Table S2); structures and energetics of the catalytic CO oxidation on $Cu_{55}(O)_{40}$ and $Cu_{55}(O)_{40}/\gamma$-Al_2O_3(100) by the Eley–Rideal (ER) mechanism (Fig. S8). See DOI: 10.1039/c9cp00974d

of several oxygen molecules or atoms on Cu catalysts have been rarely studied,[15] especially on the saturation coverage. For the CO oxidation reaction, there is still controversy regarding the oxidation state of Cu catalysts as the correlation between reactivity and oxidation states is not well established. For example, Huang *et al.* proposed that Cu_2O is the most active among the three commercial catalysts, Cu, Cu_2O, and CuO powders, under oxygen-lean and -rich conditions, and they attribute this to the high mobility of lattice oxygen.[18] In contrast, Fredriksson *et al.*[19] and Jernigan *et al.*[20] found that metallic Cu is significantly more active than Cu oxides. On Cu single-crystal surfaces, it is proposed that high oxygen coverage retards the reaction rate.[21,22] On the theoretical side, we recently investigated CO oxidation catalyzed by a Cu_{20} cluster and found that O_2 activation upon adsorption (affected by the cluster charge state) is crucial for the rate of CO oxidation.[23] To the best of our knowledge, previous calculations of CO oxidation on a Cu catalyst usually focused on low O_2 concentrations, and the effects of varying the oxygen coverage are not clear.

Typically, the Cu nanoparticles used experimentally have an average diameter of $\sim$30 nm for catalytic CO oxidation,[19] while they are in the range of 15–35 nm for copper oxide catalysts.[24,25] A smaller copper oxide catalyst with a particle size of 3.6 nm was obtained by specific preparation methods,[26] and it displays an enhanced catalytic activity. Moreover, previous studies have revealed that the CO oxidation conversion rate is considerably affected by the crystal size of the catalyst where it generally increases up to an optimal crystal size, after which the conversion rate decreases again.[27] In this article, we present the results of density functional theory (DFT) calculations for the icosahedral Cu_{55} cluster and explore the interaction of several oxygen molecules/atoms on the cluster surface, the subsequent cluster modifications, and the resulting effect on CO oxidation. Similar 55-atom clusters have been previously used as model structures for larger nanoclusters.[28] Here, the ideal icosahedral structure is the global minimum of Cu_{55} where the number of symmetrically inequivalent adsorption sites is limited. This makes it possible to examine all individual sites to find the most favorable adsorption structure, and hence, the icosahedral Cu_{55} cluster was chosen as the model structure for copper nanoparticles.

It is known that the support effects play a crucial role in the catalytic activity. Alumina is widely used as a basic catalytic support material because of its high chemical inertness, strength and hardness.[29] γ-Al_2O_3 possesses an excellent surface area owing to its small particle size, which results in high activity of the surface as a catalyst support. γ-Al_2O_3 crystals are terminated by the (100), (110) and (111) planes. The two main orientations (under practical operation conditions) of γ-Al_2O_3 facets are (100) and (110). The high-resolution images show that the (110) face is not atomically flat but significantly reconstructed. The (100) surface has the lowest surface energy, which is considered to be the most representative surface.[30] For these reasons, we have also chosen to study CO oxidation on Cu_{55}/γ-Al_2O_3(100) at different oxygen coverages. In addition, we note that in CO oxidation over metal-based catalysts, O_2 adsorption and activation is often regarded as the rate-limiting step.[31] The use of traditional PGM catalysts with inert supports such as SiO_2, Al_2O_3 and zeolites is inefficient.[32] In this type of catalyst, there is a serious competition between the adsorption and activation of CO and O_2 on the metal sites. The strong adsorption of CO seriously hinders O_2 adsorption and activation.

2. Computational methods

All electronic structure calculations were based on DFT using the spin-polarized, gradient-corrected exchange–correlation functional of Perdew, Burke, and Ernzerhof (PBE)[33] as implemented in the CP2K program package.[34,35] The single-particle Kohn–Sham wave functions were expanded by a combined Gaussian and plane wave (GPW) basis set. A molecularly-optimized double-zeta valence plus polarization (DZVP) basis set was used for the Gaussian expansion,[36] where the basis set superposition error (BSSE) has been reduced during optimization. An additional auxiliary plane wave basis with an energy cutoff of 600 Ry was used for operations involving electron density. The Cu and O valence states are $3d^{10}4s^1$ and $2s^22p^4$, respectively, and the valence electron–ion interaction is based on the analytical pseudopotentials derived by Goedecker, Teter, and Hutter (GTH).[37]

The Cu_{55} cluster with icosahedral structure is shown in Fig. S1(a) (ESI†). For the support [Fig. S1(b) and (c), ESI†], a slab model was used by cleaving the bulk γ-Al_2O_3 model[30,38] in the (100) direction. The Al_2O_3(100) support was chosen as a four-layered (4×3) slab (in total 480 atoms) and a vacuum spacing of 25 Å thickness was used within the simulation box. The top two atomic layers of the support were allowed to relax while the bottom two were fixed throughout the calculations. The Bader algorithm was used for analyzing the spatial charge decomposition among atoms.[39] The climbing image nudged elastic band (CI-NEB) method was applied for mapping the reaction pathways.[40] No symmetry constraints were imposed during structural relaxations. Vibrational analysis was performed to identify the stability of the obtained structures and zero-point energy (ZPE) corrections were included for energetics. DFT molecular dynamics (MD) calculations were performed at 300 K using a Nose thermostat[41] and the Born–Oppenheimer mode with a time step of 1 fs.

The electronic ground state of O_2 is a triplet, and correspondingly, the doublet and quartet states were examined for the Cu_{55} cluster (odd number of electrons), $Cu_{55}O_2$ (molecular adsorption), and $Cu_{55}(O)_2$ (dissociative adsorption). The spin multiplicity of Cu_{55} is a quartet, but this is only 0.03 eV lower than the doublet in total energy. On the other hand, the spin multiplicities of $Cu_{55}O_2$ and $Cu_{55}(O)_2$ are doublets, *i.e.* the adsorption complexes prefer the lowest spin state.

3. Results and discussion

3.1. Varying oxygen coverage on Cu_{55}

To study the properties of oxygen coverage on copper, we carried out a set of simulations on the Cu_{55} cluster for molecular and/or dissociative O_2 adsorption. First, the lowest-energy arrangements

of $Cu_{55}O_{2N}$ complexes were determined by sequentially adding O_2 molecules on the cluster surface (Approach 1). Here N is an integer indicating the total number of O_2 molecules adsorbed. An extensive adsorption site sampling was performed in Approach 1, where all symmetrically inequivalent sites on Cu_{55} were examined to find the most favourable adsorption structure for each step. The detailed description of the stepwise adsorption of O_2 molecules for N = 1–20 is shown in the ESI† (Fig. S2–S5). The relaxation process led to a spontaneous O_2 dissociation to atomic oxygen in several cases.

After the optimal structure was found for $Cu_{55}O_{2N}$, we computed the adsorption energy of the last molecular or dissociative adsorption as[42]:

$$E_a(N) = E(Cu_{55}O_{(2N-2)}) + E(O_2) - E(Cu_{55}O_{2N}) \quad (1)$$

where O_{2N} denotes $2N$ oxygen atoms adsorbed on Cu_{55} molecularly and/or dissociatively. $E_a(N) > 0$ indicates that the $Cu_{55}O_{2N}$ complex is more stable than the free O_2 molecule and the $Cu_{55}O_{(2N-2)}$ complex. In addition, the average adsorption energy of the added O_2 molecules was also computed as:

$$\langle E_a(N)\rangle = [E(Cu_{55}) + N \times E(O_2) - E(Cu_{55}O_{2N})]/N \quad (2)$$

By applying Approach 1, the $E_a(N)$ value becomes negative at N = 20 (Fig. S5 and Table S1, ESI†) indicating that the 20th molecule cannot adsorb exothermally (at 0 K). However, this changes if O_2 is allowed to dissociate upon adsorption. Taking into account the pronounced instability of adsorbed O_2, we decided to apply another method (Approach 2) to generate oxidized Cu_{55} geometries based on the stepwise O_2 adsorptive geometries. The initial structures of Approach 2 were based on the O_2 adsorption site scanning in Approach 1. Here, we obtained the corresponding O_2 dissociative geometries by splitting each O_2 upon adsorption one-by-one (Fig. 1; full set in Fig. S6, ESI†). The corresponding oxygen adsorption energies of Approach 2 are shown in Fig. 2.

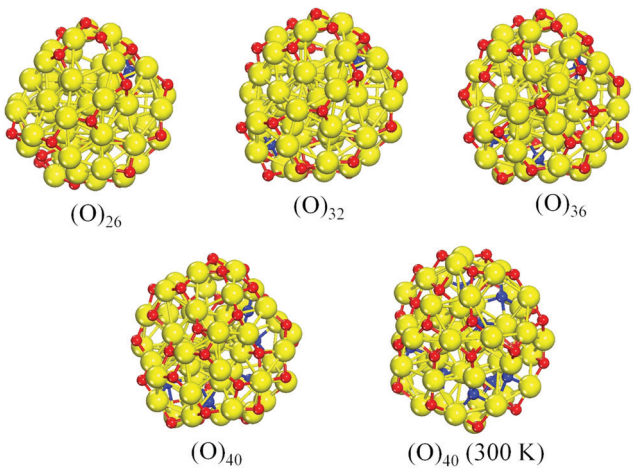

Fig. 1 Geometries of $Cu_{55}(O)_{2N}$ (N = 13, 16, 18, 20) with increasing number of endohedral oxygen atoms (blue color), as generated by Approach 2. The last structure [$Cu_{55}(O)_{40}$] is obtained after MD annealing at 300 K.

Beginning with the single molecular adsorption configuration $Cu_{55}O_2$, dissociative adsorption structures $Cu_{55}(O)_2$ were obtained by placing 2 × O atoms at different sites on the triangular facet of the 55-atom icosahedron (Approach 1). Here, two O atoms located at the nearby three-fold hollow sites is the most stable configuration [$(O)_2$ in Fig. S6, ESI†]. The second O_2 was added to $Cu_{55}(O)_2$ on the same triangular facet as the second O_2 in $Cu_{55}(O_2)_2$ (Approach 1, Fig. S3, ESI†), and the dissociated adsorption geometry was obtained in the same way as that of the first step of Approach 2 [$(O)_4$ in Fig. S6, ESI†]. The procedure was repeated with the subsequent O_2 molecules step by step until N = 20. We note that Cu_{55} undergoes a significant distortion with increasing oxygen coverage. It is possible that the high-coverage $Cu_{55}(O)_{2N}$ structures in Fig. S6 (ESI†) may not correspond to the lowest energy isomers anymore as they are based on the icosahedral Cu_{55} structure. For practical reasons, it is difficult to consider other $Cu_{55}(O)_{2N}$ structures as each composition would constitute a substantial ground-state search problem itself, and we have confined the geometry search within the icosahedral Cu_{55} motif.

Most of the dissociated O atoms are located on convex adsorption sites binding with three surface Cu atoms. However, the adsorption sites of several O atoms gradually move from convex, to surface, and to concave sites as the number of O atoms increases. As shown in Fig. 1, one O atom completely falls into an endohedral site in Cu_{55} at N = 13, forming bonds with surface and core Cu atoms. Furthermore, the endohedral O atoms increase to two at N = 16 and up to five at N = 20.

As mentioned, the structural optimizations are performed at 0 K. To see how the adsorption structure changes under more realistic reaction conditions, we carried out a DFT-MD simulation of 20 ps for $Cu_{55}(O)_{40}$ at room temperature (300 K). During this short period, the number of endohedral oxygen atoms increases up to eight (Fig. 1), which confirms the low-barrier movement of oxygen from the cluster surface towards the interior. In addition, we tested the insertion of a single oxygen atom into a clean Cu_{55} cluster. In this case, O always bounces back to the surface after optimization regardless of whether it is placed initially on a sub-surface or at the central interstitial site. This indicates that surface oxidation has to take place first before oxygen can move to the interior sites. Experimentally,[13] the interaction of oxygen with Pd nanoparticles has been studied by temperature-programmed desorption (TPD), temperature-programmed low-energy ion scattering (TP-LEIS), and X-ray photoelectron spectroscopy (XPS). A low oxygen exposure leads to surface oxygen adatoms on Pd nanoparticles. Surface O adatoms on the Pd nanoparticles move to subsurface sites starting at 400 K, and they almost all move to the sub-surface at ~750 K, desorbing only at higher temperature. High-pressure oxygen exposure readily converts small Pd nanoparticles to PdO-like species.[13]

Using eqn (1) and (2), the adsorption energies $E_a(N)$ and $\langle E_a(N)\rangle$ for Approach 2 have been calculated for the geometries in Fig. 1 and Fig. S6 (ESI†). The corresponding energies and properties are listed in Table S2 (ESI†). To see the energy changing trends clearly, $E_a(N)$ and $\langle E_a(N)\rangle$ are plotted in Fig. 2

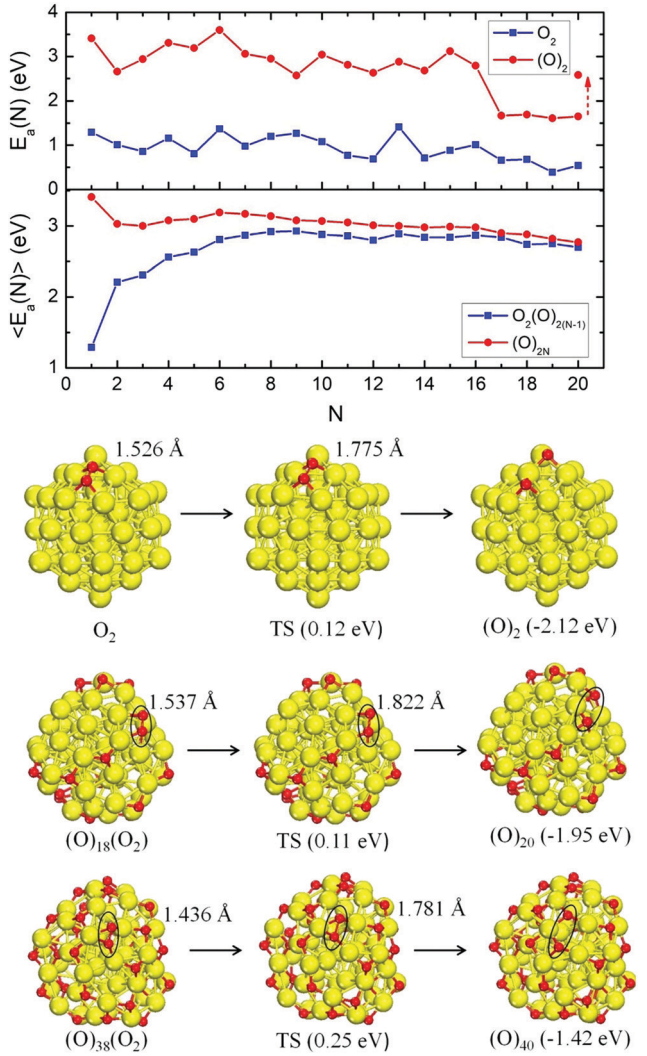

Fig. 2 Adsorption energy $E_a(N)$ of O_2 upon molecular (O_2) or dissociative $(O)_2$ adsorption on Cu_{55} and the corresponding average adsorption energy $\langle E_a(N)\rangle$ of added O_2 molecules (Approach 2, top). The separate point is the $E_a(N)$ of MD simulation for N = 20. The structures of the initial state (IS), transition state (TS), and final state (FS) of the reaction pathways for $O_2 \rightarrow O + O$ on $Cu_{55}O_{2N}$ (N = 1, 10, 20) together with the energy changes with respect to the IS (below). The bond lengths of the reactive O_2 molecules are included.

for both molecular and atomic adsorption. The dissociative O_2 adsorption is energetically much more favorable than molecular adsorption: $E_a(N)$ is above 2.5 eV for dissociative adsorption until N = 16, which is much higher than 1.4 eV for the highest value of O_2 molecular adsorption. For N = 17–20, $E_a(N)$ decreases down to 1.6 eV for $(O)_2$ adsorption, which is still significantly higher than O_2 adsorption (<0.7 eV). The decrease of $E_a(N)$ for $N \geq 17$ is consistent with the energy changing trend in Fig. S5 (Approach 1, ESI†), and it is due to a large oxygen concentration on the cluster surface. Our MD simulations for N = 20 reveal that oxygen diffusion to endohedral sites causes an increase in the $E_a(N)$ value to 2.58 eV, *i.e.* back to the original level (Fig. 2). However, one cannot observe any saturation at N = 20 in Approach 2 as $E_a(N)$ does not change the sign. For the corresponding geometry of $Cu_{55}(O)_{40}$, each triangular facet of Cu_{55} has two oxygen atoms. Evidently, it is possible to add even more oxygen to the cluster but we did not pursue further towards the fully saturated $Cu_{55}(O)_{2N}$ due to the computational demands.

For the average adsorption energy $\langle E_a(N)\rangle$, the fully dissociated adsorption $(O)_{2N}$ is also higher than the adsorption with a molecule, *i.e.* $O_2(O)_{2(N-1)}$, and they approach each other with N. At the same time, the net charge transfer increases with the number of dissociated oxygen atoms (Table S2, ESI†). The average $\langle$Cu–Cu$\rangle$ bond length in $Cu_{55}(O)_{2N}$ is larger than that in $Cu_{55}O_2(O)_{2(N-1)}$ for each number of N (Table S2, ESI†), and the Cu binding O atoms distort the Cu_{55} geometry severely.

Obviously, O_2 is very unstable on Cu_{55}, and we have simulated the O–O bond cleavage with respect to the geometries in Fig. S6 (ESI†). The geometries of the reactant, the transition state (TS), and the product of the reaction paths are shown in Fig. 2 where N = 1, 10 and 20 have been chosen as the representative cases. The initial O_2 adsorption results in activation (elongation) of the O–O bond to the super-oxo state, and the calculated dissociative reaction barriers (TS) are small on all clusters as shown in Fig. 2; the highest barrier at N = 20 is only 0.25 eV. The barrier height correlates inversely with the O–O bond elongation and charge transfer from Cu_{55} to O_2. These results show that O_2 can be effectively activated on Cu_{55} regardless of the oxygen coverage (within the studied range).

3.2. CO oxidation at different oxygen coverages

Our previous study[23] has demonstrated that CO oxidation proceeds efficiently on Cu_{20} when O_2 is pre-adsorbed in a dissociative manner. The results in Section 3.1 also show that O_2 dissociates easily on the Cu_{55} cluster at different oxygen coverages. In addition, experimental studies[20–22] have suggested that CO oxidation takes place between adsorbed CO molecules and O atoms, following the Langmuir–Hinshelwood (L–H) mechanism. To check the effect of oxygen coverage, we have studied CO oxidation in the presence of fully dissociated O_2 atoms.

3.2.1. Reaction mechanism on $Cu_{55}(O)_{2N}$. The initial state (IS) of the reaction was obtained by adding CO to $Cu_{55}(O)_{2N}$. The CO adsorption sites are explored within the triangular facet of Cu_{55} which is the one with the last dissociated 2 × O atoms. The Cu top site is always the most stable for CO adsorption. In contrast to O_2, the C═O bond is hardly influenced upon adsorption (isolated 1.14 Å, max. 1.16 Å on the cluster). Again N = 1, 10 and 20 are chosen to represent the oxygen coverage from low to high. For N = 20, the annealed geometry from the DFT-MD simulation at 300 K is used which is 0.63 eV more stable than the relaxed starting structure at 0 K.

The catalytic reaction pathways for CO oxidation on $Cu_{55}(O)_{2N}$ are shown in Fig. 3. Upon the reaction, CO and the nearest O move closer to each other, followed by a crossing of the energy barrier (TS) to form an intermediate (IM) complex. Subsequent to the IM complex, there is a barrier-free release of the formed CO_2 molecule. The activation energy barriers decrease as the oxygen coverage increases, while at the same time, the adsorption energies of CO in the corresponding IS also decrease (1.09 eV, 0.83 eV, and 0.78 eV, respectively). Moreover, the binding energies of O in the neighboring

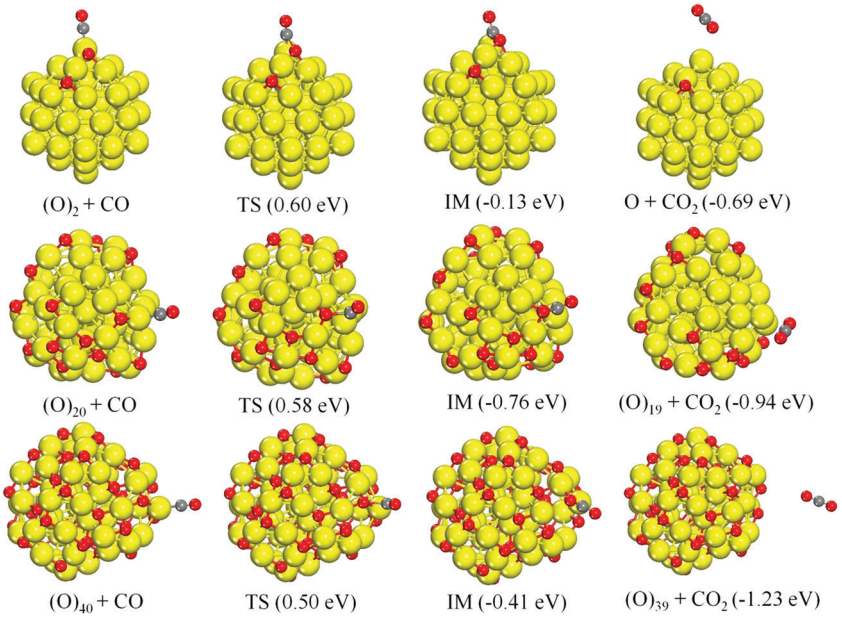

Fig. 3 Reaction pathways of CO oxidation on $Cu_{55}(O)_{2N}$ (N = 1, 10, and 20). The corresponding structures of the initial state (IS), transition state (TS), intermediate (IM), and final state (FS) are shown. The energy changes are with respect to the IS.

site of CO exhibit a similar changing trend to CO adsorption (Table S2, ESI†). Correspondingly, at high oxygen coverage, the adsorbed CO and neighboring O are more weakly bound to Cu_{55} giving rise to a more efficient reaction rate. According to CO oxidation experiments on Ru(0001),[11] it has been identified that the highest rates of CO_2 production occurred for high oxygen partial pressures and concomitantly high oxygen coverages.

In addition, the d-band centers (C_d) of the selected $Cu_{55}(O)_{2N}$ clusters in Fig. 3 were calculated from the electronic densities of states, DOS (Fig. S7, ESI†). The C_d values are −2.44, −2.66, and −2.78 eV, respectively, displaying a downward shift with oxygen coverage due to the increased charge transfer from Cu_{55}. From the above results, we can see that CO oxidation benefits from increasing oxygen coverage, while the d-band center and the CO and O binding energies are reduced.

3.2.2. Reaction mechanism on $Cu_{55}(O)_{2N}/\gamma$-$Al_2O_3(100)$. The $Cu_{55}(O)_{2N}/\gamma$-$Al_2O_3(100)$ (N = 1, 10 and 20) geometries have been obtained by placing the $Cu_{55}(O)_{2N}$ clusters on a γ-$Al_2O_3(100)$ support. These geometries are considered as a representative model of soft-landed $Cu_{55}(O)_{2N}$ on a γ-$Al_2O_3(100)$ substrate. The Wulff–Kaishew construction effect was not included because it would require a completely new set of results for the substrate-modified cluster structure. Here, we have examined several orientations of the $Cu_{55}(O)_{2N}$ clusters to locate the energetically most favorable support configurations within the soft-landing regime (Fig. 4). The support binding energies (E_b) of $Cu_{55}(O)_{2N}$ on γ-$Al_2O_3(100)$ were computed as:

$$E_b(N) = E(Cu_{55}O_{2N}) + E(Al_2O_3) - E(Cu_{55}O_{2N}/Al_2O_3) \quad (3)$$

where $E(X)$ is the total energy of the corresponding system X. To visualize the interaction between $Cu_{55}(O)_{2N}$ clusters and γ-$Al_2O_3(100)$, Fig. 4 also shows the charge density differences (CDDs) of the systems. CDD is calculated as:

$$\Delta\rho = \rho(Cu_{55}O_{2N} + Al_2O_3) - \rho(Cu_{55}O_{2N}) - \rho(Al_2O_3) \quad (4)$$

where $\rho(X)$ is the electron density of system X. The binding energies, geometric parameters, and the net charge transfer from the substrate to the cluster are listed in Table 1.

As expected, the $Cu_{55}(O)_{2N}$ clusters become more distorted on the Al_2O_3 substrate (Fig. 4). The number of oxygen atoms at the $Cu_{55}(O)_{2N}/Al_2O_3$ interface increases from 1 to 3, then to 6 as N increases. The interfacial oxygen atoms are closer to the Al_2O_3 surface than Cu atoms. The Cu–O bond lengths across the interface are always greater than 2.0 Å, while the O–Al bonds increase from 1.83 Å to 1.91 Å (Table 1), *i.e.* the distance between the cluster and substrate increases with N. The corresponding binding energies decrease from 2.87 eV to 2.17 eV, and CDDs in Fig. 4 show how the interaction at the cluster–support interface changes as there is more weight on the cluster itself for $Cu_{55}(O)_{40}$. According to the Bader charge analysis (Table 1), $Cu_{55}(O)_2$ carries a positive net charge, which indicates that the cluster has transferred 0.22 electron to the γ-$Al_2O_3(100)$ surface. The other two systems carry about 0.5 e negative net charge, each, indicating charge transfer from the support. On the whole, the charge transfer between $Cu_{55}(O)_{2N}$ and Al_2O_3 is weak, which is consistent with the previous reports[43,44] where charge transfers of similar magnitude were reported. For example, the net charge of Cu is 0.08 e and 0.15 e, respectively, for the Cu_2 cluster adsorbed on Al_2O_3[43] and ZnO[44] surfaces. In addition, it has been reported[43] that the charge may be locally transferred from Cu to the Al_2O_3 carrier, and the transfer of electron charge further decreases during Cu deposition.

To understand how the electronic structure is modified due to oxygen coverage, we have performed a detailed analysis of

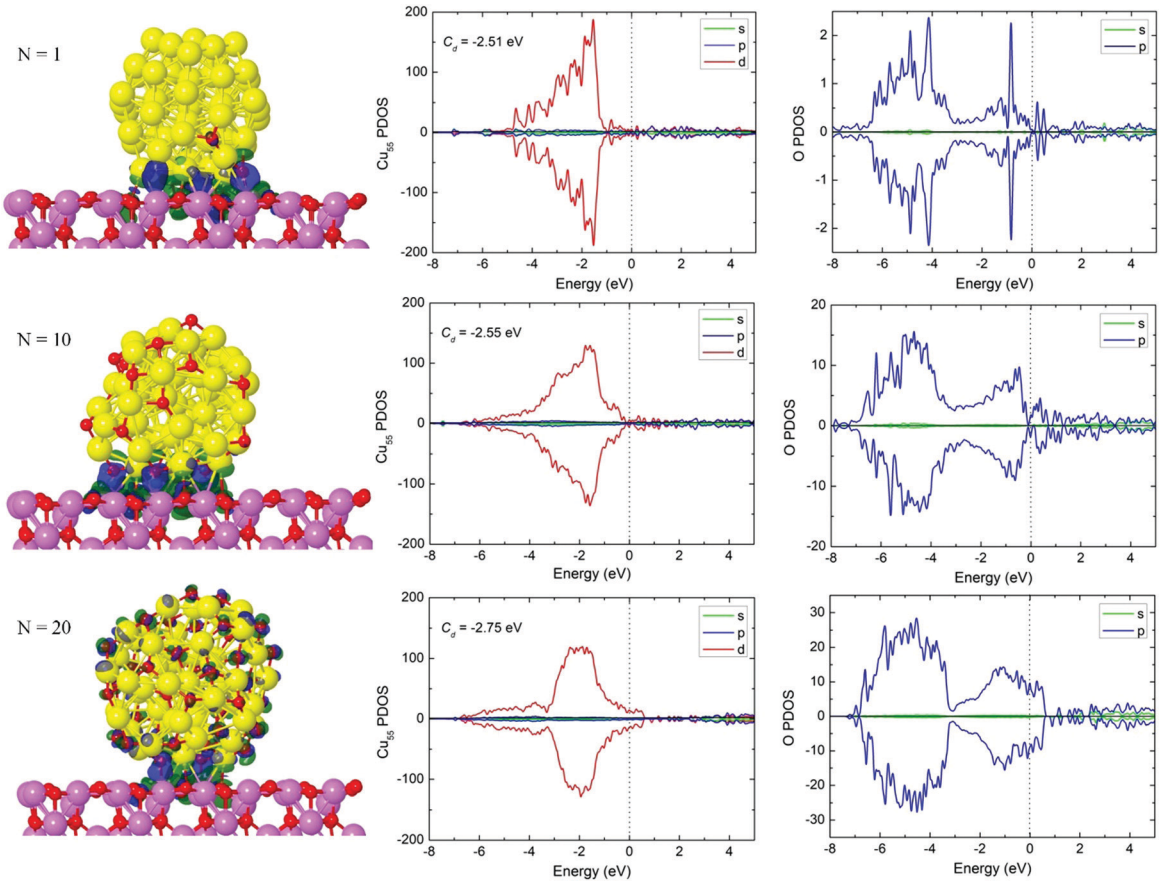

Fig. 4 Optimized $Cu_{55}(O)_{2N}/\gamma$-$Al_2O_3(100)$ (N = 1, 10, 20) geometries and charge density differences (CDDs) of the $Cu_{55}(O)_{2N}$ clusters adsorbed on γ-$Al_2O_3(100)$. Green and blue colors represent charge depletion and accumulation, respectively. The isosurface values are ± 0.002 e Å^{-3} (left column). Spin-polarized projected density of states (PDOS) of Cu_{55} with $(O)_{2N}$ coverage for the $Cu_{55}(O)_{2N}/\gamma$-$Al_2O_3(100)$ system. The PDOS are projected onto the Cu atoms in Cu_{55} (middle column) and the O atoms in the coverage (right column). The dotted line represents the Fermi level at 0 eV.

Table 1 Binding energy (E_b) of $Cu_{55}(O)_{2N}$ on the γ-$Al_2O_3(100)$ support, charge on the cluster (Q), the nearest bond length of O–Al (r_{O-Al}) at the interface, adsorption energy (E_{ad}) of CO, and activation energy barrier of CO oxidation (E_r)

$Cu_{55}(O)_{2N}/\gamma$-$Al_2O_3(100)$	E_b (eV)	Q (e)	r_{O-Al} (Å)	E_{ad} (eV)	E_r (eV)
N = 1	2.87	0.22	1.83	1.06	0.57
N = 10	2.76	−0.56	1.86	1.00	0.65
N = 20	2.71	−0.49	1.91	0.87	0.59

the Kohn–Sham states by examining the projected density of states (PDOS) from the contribution of different atom-centered orbital components (s, p, d). Fig. 4 shows the PDOS of Cu_{55} with $(O)_{2N}$ (N = 1, 10, and 20) coverage on γ-$Al_2O_3(100)$. PDOS is projected with respect to the Cu atoms in the cluster and O atoms in the coverage, and the spin-up and spin-down contributions are plotted separately (paramagnetic system). PDOS shows an interesting overall evolution at the Fermi energy where both Cu_{55} and oxygen weights gradually increase with oxidation such that the N = 20 case exhibits an enhanced metallic character. The electronic states near the Fermi energy have a major influence on the p states of O atoms, and the underlying valence band PDOS corresponds mainly to the atomic d states of Cu_{55}. Thus, the bonding of O atoms with Cu results in a strong hybridization between the O p-states and the Cu d-states. Moreover, the d-band center (C_d) is also shown in Fig. 4. The d-band center moves downward with an increase in the oxygen coverage, which is similar to the isolated $Cu_{55}(O)_{2N}$ clusters (Fig. S7, ESI†). For N = 1, the C_d value decreases to −2.51 eV compared to the −2.44 eV in the isolated $Cu_{55}(O)_2$ cluster which is related to the charge transfer from $Cu_{55}(O)_2$ to the substrate. In contrast, the C_d values increase for the other two systems (−2.55 eV and −2.75 eV) in comparison with the isolated clusters. The reason is that $Cu_{55}(O)_{2N}$ receive electron density from the support in these cases, which lifts the d-band center closer to the Fermi level.

The catalytic reaction pathways and CO oxidation energetics are shown in Fig. 5. The reaction paths are similar to those on the isolated $Cu_{55}(O)_{2N}$ clusters (Fig. 3). The activation energy barriers are 0.57 eV, 0.65 eV and 0.59 eV for N = 1, 10 and 20, respectively. The CO adsorption energies for the corresponding IS are 1.06 eV, 1.00 eV and 0.87 eV, respectively, showing a gradual decrease *versus* the number of oxygen atoms. The CO oxidation activation energy barriers are of the same magnitude as that of the isolated $Cu_{55}(O)_{2N}$ clusters. For N = 10 and 20, the reaction barriers are slightly higher (by $<$0.1 eV) and this

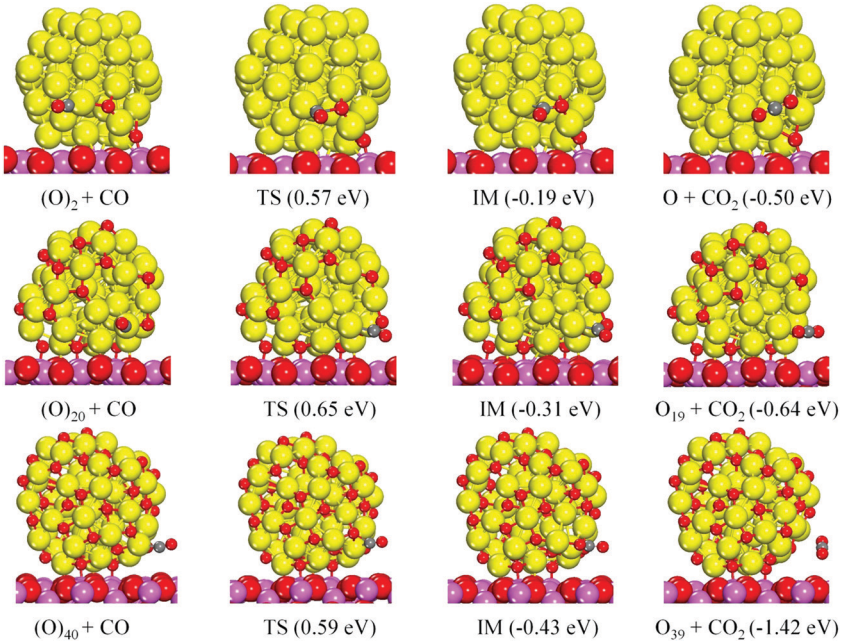

Fig. 5 Structures of the initial state (IS), transition state (TS), intermediate (IM), and final state (FS) for the catalytic CO oxidation on $Cu_{55}(O)_{2N}/\gamma$-$Al_2O_3(100)$ (N = 1, 10, 20) and the energy changes with respect to the IS.

correlates with the larger CO adsorption energy for the supported clusters. Here, the charge transfer from Al_2O_3 to $Cu_{55}(O)_{2N}$ (N = 10 and 20) increases the adsorption strength of CO, which slightly increases the reaction barrier.

Finally, we remark that some experiments[20–22] indicate that the reaction order of oxygen is negative over metallic Cu, which is due to the fact that adsorbed atomic O interacts strongly with the metal surface and blocks the active sites so that CO cannot adsorb. However, there is also opposite evidence[11] which shows that the reaction with CO_2 at high gas pressures occurs both *via* scattering of gas-phase CO molecules and by CO molecules weakly adsorbed at vacancies in the oxygen adlayer, *i.e.* the Eley–Rideal (E–R) mechanism contributes to the reaction. Here, we tested the E–R mechanism for $Cu_{55}(O)_{40}$ and $Cu_{55}(O)_{40}/\gamma$-$Al_2O_3(100)$ (Fig. S8, ESI†), and the reaction barriers are clearly higher than those for the L–H mechanism. In our calculations, as the oxygen coverage increases up to N = 20, the adsorbed CO molecule and the neighboring O atom come close to one another while binding more weakly on Cu_{55}, and this is reflected in the modest reaction barrier height.

4. Conclusion

We have systematically studied the adsorption of several (N = 1–20) oxygen molecules on the icosahedral Cu_{55} cluster using the spin-polarized DFT calculations. Herein, we must emphasize the representative nature of the $Cu_{55}(O)_{2N}$ clusters obtained, as it is very difficult to obtain the true ground states for such numbers of atoms *via* DFT calculations. Based on these model structures, we focus on the behavior of oxygen on Cu_{55}, cluster–support interaction, and the effects of oxygen coverage on CO oxidation.

As the oxygen coverage increases, several adsorbed O atoms gradually move from convex sites, to surface, and to concave sites. The first O atom that spontaneously relaxes to an endohedral site of Cu_{55} is observed at N = 13. Furthermore, the endohedral O atoms increase with greater oxygen exposure. The O–O bond cleavage processes on Cu_{55} with varying numbers of oxygen atoms are analyzed, and it is observed that O_2 gets activated upon adsorption and it dissociates either spontaneously or with a very small barrier. A short DFT-MD simulation (20 ps) at 300 K confirms the small dissociation barrier and the active movement of oxygen atoms from the surface to the interior sites at larger oxygen coverages. Furthermore, CO oxidation reactions have been studied on $Cu_{55}(O)_{2N}$ and $Cu_{55}(O)_{2N}/\gamma$-$Al_2O_3(100)$ (N = 1, 10, and 20) systems with fully dissociated oxygen molecules. For $Cu_{55}(O)_{2N}/\gamma$-$Al_2O_3(100)$, the interaction between the cluster and the substrate decreases as the distance between them increases with the number of oxygen atoms, N, and the charge transfer across the $Cu_{55}(O)_{2N}/Al_2O_3$ interface is weak. The CO oxidation reaction order is positive over oxygen coverage on both $Cu_{55}(O)_{2N}$ and $Cu_{55}(O)_{2N}/\gamma$-Al_2O_3 systems with similar reaction barrier heights (0.50–0.65 eV). This is due to the inherently small adsorption energies of the reactants and their modest variation as a function of the varying oxygen coverage and the presence of the Al_2O_3 support.

Finally, it should be noted that the range of adsorbed oxygen is still limited in this work. The Cu_{55} cluster reaches a maximum content of 40 oxygen atoms (*i.e.* beyond Cu_2O but not yet at CuO), and, as evidenced by the results (small number of endohedral O atoms; modest reaction barriers), it appears that the cluster can host even more oxygen without losing its catalytic activity. In particular, it is likely that the number of endohedral oxygen atoms will increase further with increasing oxygen content.

Conflicts of interest

There are no conflicts of interest to declare.

Acknowledgements

DFT calculations were carried out at CSC – the IT Center for Science Ltd, Espoo, Finland. Financial support has been provided by the European Union Horizon 2020 NMP programme through the CritCat Project under Grant Agreement No. 686053.

References

1 X. Huang, S. Tang, X. Mu, Y. Dai, G. Chen, Z. Zhou, F. Ruan, Z. Yang and N. Zheng, *Nat. Nanotechnol.*, 2011, **6**, 28–32.
2 L. Hu, X. Cao, D. Ge, H. Hong, Z. Guo, L. Chen, X. Sun, J. Tang, J. Zheng, J. Lu and H. Gu, *Chem. – Eur. J.*, 2011, **17**, 14283–14287.
3 C. Chiu, P. Chung, K. Lao, C. Liao and M. Huang, *J. Phys. Chem. C*, 2012, **116**, 23757–23763.
4 N. Iwasa, S. Arai and M. Arai, *Appl. Catal., B*, 2008, **79**, 132–141.
5 Y. Chan and J. Chen, *Appl. Surf. Sci.*, 2016, **387**, 16–27.
6 T. Bell and L. Torrente-Murciano, *Top. Catal.*, 2016, **59**, 1438–1457.
7 S. De, J. Zhang, R. Luque and N. Yan, *Energy Environ. Sci.*, 2016, **9**, 3314–3347.
8 A. M. Hengne and C. V. Rode, *Green Chem.*, 2012, **14**, 1064–1072.
9 C. Zhou, J. N. Beltramini, C. Lin, Z. Xu, G. Q. Lu and A. Tanksale, *Catal. Sci. Technol.*, 2011, **1**, 111–122.
10 M. Behrens, F. Studt, I. Kasatkin, S. Kuhl, M. Havecker, F. Abild-Pedersen, S. Zander, F. Girgsdies, P. Kurr, B. Kniep, M. Tovar, R. W. Fischer, J. Norskov and R. Schlogl, *Science*, 2012, **336**, 893–897.
11 C. Stampfl and M. Scheffler, *Surf. Sci.*, 1997, **377**, 808–812.
12 J. Gustafson, S. Blomberg, N. M. Martin, V. Fernandes, A. Borg, Z. Liu, R. Chang and E. Lundgren, *J. Phys.: Condens. Matter*, 2014, **26**, 055003.
13 S. Penner, P. Bera, S. Pedersen, L. T. Ngo, J. J. W. Harris and C. T. Campbell, *J. Phys. Chem. B*, 2006, **110**, 24577–24584.
14 H. Zhou, X. Chen and J. Wang, *Int. J. Quantum Chem.*, 2016, **116**, 939–944.
15 X. Yuan, L. Liu, X. Wang, M. Yang, K. Jackson and J. Jellinek, *J. Phys. Chem. A*, 2011, **115**, 8705–8712.
16 E. Fernández, M. Boronat and A. Corma, *J. Phys. Chem. C*, 2015, **119**, 19832–19846.
17 E. Florez, W. Tiznado, F. Mondragón and P. Fuentealba, *J. Phys. Chem. A*, 2005, **109**, 7815–7821.
18 T. Huang and D. Tsai, *Catal. Lett.*, 2003, **87**, 173–178.
19 Y. Bu, J. Niemantsverdriet and H. Fredriksson, *ACS Catal.*, 2016, **6**, 2867–2876.
20 G. Jernigan and G. Somorjai, *J. Catal.*, 1994, **147**, 567–577.
21 M. Domagala and C. Campbell, *Catal. Lett.*, 1991, **9**, 65–70.
22 J. Szanyi and D. Goodman, *Catal. Lett.*, 1993, **21**, 165–174.
23 L. Ma, M. Melander, K. Laasonen and J. Akola, *Phys. Chem. Chem. Phys.*, 2015, **17**, 7067–7076.
24 A. Zedan, A. Mohamed, M. El-Shall, S. AlQaradawi and A. AlJaber, *RSC Adv.*, 2018, **8**, 19499–19511.
25 H. Elazab, *Biointerface Res. Appl. Chem.*, 2018, **8**, 3278–3281.
26 L. Gong, L. Luo, R. Wang and N. Zhang, *J. Chil. Chem. Soc.*, 2012, **57**, 1048–1053.
27 N. Soliman, *J. Mater. Res. Technol.*, 2019, DOI: 10.1016/j.jmrt.2018.12.012.
28 D. Tang and J. Zhang, *RSC Adv.*, 2013, **3**, 15225–15236.
29 M. Trueba and S. Trasatti, *Eur. J. Inorg. Chem.*, 2005, 3393–3403.
30 M. Digne, P. Sautet, P. Raybaud, P. Euzen and H. Toulhoat, *J. Catal.*, 2004, **226**, 54–68.
31 D. Widmann and R. Behm, *Acc. Chem. Res.*, 2014, **47**, 740–749.
32 J. Lin, X. Wang and T. Zhang, *Chin. J. Catal.*, 2016, **37**, 1805–1813.
33 J. Perdew, K. Burke and M. Ernzerhof, *Phys. Rev. Lett.*, 1996, **77**, 3865.
34 J. VandeVondele, M. Krack, F. Mohamed, M. Parrinello, T. Chassaing and J. Hutter, *Comput. Phys. Commun.*, 2005, **167**, 103–128.
35 CP2K version 2.5. CP2K is freely available from http://www.cp2k.org.
36 J. VandeVondele and J. Hutter, *J. Chem. Phys.*, 2007, **127**, 114105.
37 S. Goedecker, M. Teter and J. Hutter, *Phys. Rev. B: Condens. Matter Mater. Phys.*, 1996, **54**, 1703.
38 M. Honkanen, J. Wang, M. Kärkkäinen, M. Huuhtanen, H. Jiang, K. Kallinen, R. L. Keiski, J. Akola and M. Vippola, *J. Catal.*, 2018, **358**, 253–265.
39 M. Yu and D. Trinkle, *J. Chem. Phys.*, 2011, **134**, 064111.
40 G. Henkelman, B. Uberuage and H. Jónsson, *J. Chem. Phys.*, 2000, **113**, 9901–9904.
41 S. A. Nosé, *J. Chem. Phys.*, 1984, **81**, 511.
42 A. Pelzer, J. Jellinek and K. Jackson, *J. Phys. Chem. A*, 2015, **119**, 3594–3603.
43 Z. Zuo, L. Wang, P. Han and W. Huang, *Appl. Surf. Sci.*, 2014, **290**, 398–404.
44 Z. Zuo, P. Han, Z. Li, J. Hu and W. Huang, *Appl. Surf. Sci.*, 2012, **261**, 640–646.